Metastable Phase Diagram of Nanocrystalline $ZrO_2-Sc_2O_3$ Solid Solutions

Paula M. Abdala,[†] Aldo F. Craievich,[‡] Marcia C. A. Fantini,[‡] Marcia L. A. Temperini,[§] and Diego G. Lamas*,[†]

Centro de Investigaciones en Sólidos (CINSO), CITEFA-CONICET, J. B. de La Salle 4397, B1603ALO Villa Martelli, Pcia. de Buenos Aires, Argentina, Instituto de Física, Universidade de São Paulo, Travessa R da Rua do Matão 187, Cidade Universitária, 05508-900 São Paulo, SP, Brazil, and Instituto de Química, Universidade de São Paulo, Av. Prof. Lineu Prestes 748, Cidade Universitária, 05508-900 São Paulo, SP, Brazil

Received: May 16, 2009; Revised Manuscript Received: September 17, 2009

We have investigated the crystal structures and phase transitions of nanocrystalline ZrO_2-1 to -13 mol % Sc_2O_3 by synchrotron X-ray powder diffraction and Raman spectroscopy. $ZrO_2-Sc_2O_3$ nanopowders were synthesized by using a stoichiometric nitrate−lysine gel−combustion route. Calcination processes at 650 and at 850 °C yielded nanocrystalline materials with average crystallite sizes of (10 ± 1) and (25 ± 2) nm, respectively. Only metastable tetragonal forms and the cubic phase were identified, whereas the stable monoclinic and rhombohedral phases were not detected in the compositional range analyzed in this work. Differently from the results of investigations reported in the literature for $ZrO_2-Sc_2O_3$ materials with large crystallite sizes, this study demonstrates that, if the crystallite sizes are small enough (in the nanometric range), the metastable t″-form of the tetragonal phase is retained. We have also determined the t′−t″ and t″−cubic compositional boundaries at room temperature and analyzed these transitions at high temperature. Finally, using these results, we built up a metastable phase diagram for nanocrystalline compositionally homogeneous $ZrO_2-Sc_2O_3$ solid solutions that strongly differs from that previously determined from compositionally homogeneous $ZrO_2-Sc_2O_3$ solid solutions with much larger crystallite sizes.

Introduction

$ZrO_2-Sc_2O_3$ ceramics are considered as promising candidates for solid electrolytes in solid oxide fuel cells and other electrochemical devices because they have the highest oxide ionic conductivity among all ZrO_2-based materials. Many ZrO_2-based solid solutions exhibit several stable and metastable phases depending on composition, temperature, and average crystallite sizes. Since the electrical properties of $ZrO_2-Sc_2O_3$ solid solutions strongly depend on their type of structure, the study of the phase diagram of this system is of great importance.

Depending on composition and temperature, polycrystalline $ZrO_2-Sc_2O_3$ solid solutions composed of large (non-nanometric) crystallites exhibit monoclinic, tetragonal, cubic, or rhombohedral (β, γ, and δ) phases.[1] The tetragonal and cubic phases have excellent electrical properties, whereas the performance of the monoclinic and rhombohedral phases is poor. The phase diagram of $ZrO_2-Sc_2O_3$ proposed by Ruh et al.[2] is generally accepted, even though several details are still under discussion.

In compositionally homogeneous ZrO_2-based solid solutions, the tetragonal phase can exhibit three forms, known as t, t′, and t″.[1] The stable tetragonal form is called the t-form. The t′-form has a wider solubility but is unstable in comparison with the mixture of t-form and cubic phase. Finally, the t″-form has an axial ratio, *c*/*a*, of unity, with the oxygen atoms displaced along the *c* axis from their ideal sites of the cubic phase. In most of ZrO_2-based systems, as the dopant content increases, the tetragonal structure gradually changes to the cubic one, exhibiting t′ ↔ t″ and t″ ↔ cubic transitions. However, Yashima and co-workers proposed a metastable phase diagram for compositionally homogeneous $ZrO_2-Sc_2O_3$ materials of large average crystallite sizes without the presence of the metastable t″-form.[1,3] Differently, these authors concluded that, for solid solutions with Sc_2O_3 contents between 10 and 12 mol %, the rhombohedral β phase coexists with the cubic one.[1,3] The retention of the t″-form in this system has only been reported by Xu et al. in nanopowders synthesized by a two-step hydrothermal process.[4] However, these authors only identified the t″-form by Raman spectroscopy; thus, a more detailed crystallographic study of nanocrystalline compositionally homogeneous $ZrO_2-Sc_2O_3$ solid solutions is still missing.

In this work, we investigated the phase diagram of compositionally homogeneous $ZrO_2-Sc_2O_3$ nanopowders synthesized by a gel−combustion route and determined their crystal structure as a function of Sc_2O_3 content (up to 13 mol %). Samples with two average crystallite sizes, $\langle D \rangle = (10 \pm 1)$ and $\langle D \rangle = (25 \pm 2)$ nm, were analyzed. We also carried out a structural study of the ZrO_2-10 mol % Sc_2O_3 solid solution, with $\langle D \rangle = 25$ nm, at high temperature. Taking into account these results corresponding to samples with $\langle D \rangle = 25$ nm, together with those reported in a previous study at high temperature of ZrO_2-8 and -11 mol % Sc_2O_3 solid solutions with the same average crystallite size,[5] we built up the ZrO_2-rich side of the metastable phase diagram for nanocrystalline $ZrO_2-Sc_2O_3$ solid solutions.

Experimental Methods

Synthesis of Nanocrystalline $ZrO_2-Sc_2O_3$ Solid Solutions. Nanocrystalline ZrO_2-1 to -13 mol % Sc_2O_3 powders were synthesized by a previously developed stoichiometric nitrate−lysine gel−combustion process.[5] $ZrO(NO_3)_2 \cdot 6H_2O$ (Alpha Aesar, U.S.A., 99.9%) and $Sc(NO_3)_3 \cdot 4H_2O$ (Standford Materials, U.S.A., 99.99%) were dissolved in distilled water in the

* To whom correspondence should be addressed. E-mail: dlamas@citefa.gov.ar.
[†] CITEFA-CONICET.
[‡] Instituto de Física.
[§] Instituto de Química.

10.1021/jp904584e CCC: $40.75
Published on Web 10/07/2009

corresponding ratio to the desired final composition. Lysine (Merck, Germany) was added in the stoichiometric proportion for the redox reaction. The solution was concentrated by thermal evaporation in a hot plate at 200 °C. A viscous gel was formed and then burnt out as a result of an exothermic reaction. The system remained homogeneous during the whole process, and no precipitation was observed. As-reacted materials were calcined in air at 650 °C for 2 h in order to remove the carbonaceous residues. Samples treated at 850 °C for 1 h were also investigated.

Synchrotron X-ray Powder Diffraction. The phases present in all samples and their crystal structure were studied by synchrotron X-ray powder diffraction (SXPD). The experiments were carried out at the D10B-XPD beamline of the Brazilian Synchrotron Light Laboratory (LNLS, Campinas, Brazil),[6] employing a high-intensity (low-resolution) configuration, without crystal analyzer.[7–9] This high photon flux configuration has demonstrated to be very useful for the measurement of extremely weak Bragg peaks, thus allowing us to discriminate between the tetragonal and cubic phases. In addition, as we will see in the next sections, the knowledge of the integral of very weak Bragg peaks related to displacements of oxygen atoms in tetragonal solid solutions allowed us to precisely determine the fractional *z*-coordinate of the oxygen atom in the asymmetric unit of the tetragonal unit cell, *z*(O).[7–9] The wavelength of the X-ray beam was set at 1.5495 Å. The average crystallite sizes of the powdered samples were determined from the width of the profile of Bragg reflections by applying the Scherrer equation.[10]

In order to determine the lattice parameters, *a* and *c*, and the axial ratio, *c*/*a*, as functions of Sc_2O_3 content, Rietveld refinements were performed by using the program FullProf.[11] For the tetragonal phase, the $P4_2/nmc$ space group was assumed, with (Zr^{4+}; Sc^{3+}) cations and O^{2-} anions in 2a and 4d positions, respectively. The results of these refinements were given in terms of the usual pseudofluorite unit cell ($a \approx c$).[12] For the cubic phase (fluorite-type crystal structure), the $Fm\bar{3}m$ space group was assumed, with (Zr^{4+}; Sc^{3+}) cations and O^{2-} anions in 4a and 8c positions, respectively. The Bragg peak shape was assumed to be well-represented by a pseudo-Voigt function. The background of each profile was adjusted by a six-parameter polynomial function in $(2\theta)^n$, $n = 0-5$. Isotropic atomic temperature parameters were used. The thermal parameters corresponding to Zr and Sc atoms were assumed to be equal.

As discussed in previous works,[7–9] Rietveld analysis is not accurate enough for the determination of the fractional z-coordinate of the oxygen atom in the asymmetric unit of the tetragonal unit cell, *z*(O), in the tetragonal solid solutions, since the whole XPD pattern is fitted and, therefore, the effect of relevant but very weak peaks is underestimated. Therefore, we have determined the *z*(O) coordinate from the ratio of the integrated intensities of the weak 112 Bragg peak and the strong 111 one (*I*(112) and *I*(111), respectively) by using the following equation:[7–9]

$$\frac{I(112)}{I(111)} = \frac{4{f_O}^2 \sin^2(4\pi z(O)){q_O}^2 L_{112}}{{f_{Zr-Sc}}^2 {q_{Zr-Sc}}^2 L_{111}} \quad (1)$$

where f_{Zr-Sc} is the average atomic scattering factor of Zr^{4+} and Sc^{3+} cations, q_{Zr-Sc} is their average temperature factor, f_O is the atomic scattering factor of O^{2-} anion, q_O is its temperature factor, and L_{112} and L_{111} are the Lorentz factors corresponding to 112 and 111 Bragg peaks. For a symmetric $\theta-2\theta$ scan, $L(\theta) = \cos(\theta)/\sin^2(2\theta)$.

The D10B-XPD beamline of the LNLS is equipped with a furnace that enables in situ investigation of phase transitions. In this way, we have studied the ZrO_2-10 mol % Sc_2O_3 sample calcined at 850 °C, using the same procedure as that described above. In a previous work, we have investigated the same phase transitions in ZrO_2-8 and -11 mol % Sc_2O_3 solid solutions.[5]

Raman Spectroscopy. Raman spectroscopy was applied to identify the phases present at room temperature in all samples, particularly for compositions close to the t″−cubic boundary. Raman spectra were recorded in a Renishaw imaging microscope system 3000 spectrophotometer equipped with an Olympus BH-2 microscope and a CCD detector. A 632.8 nm He−Ne laser line (Spectra Physics, model 127) was used as excitation radiation. The final analyzed spectra were averages of five subsequent scans of 20 s each.

Results and Discussion

Qualitative Analysis and Crystal Structure at Room Temperature. Figure S1 (see the Supporting Information) displays the SXPD patterns corresponding to selected samples calcined at 650 °C. The patterns from the other nanopowders exhibited similar overall features. All the samples were single-phased and exhibited very similar average crystallite sizes, $\langle D \rangle = (10 \pm 1)$ nm. Depending on composition, each sample exhibited only one phase, namely, tetragonal t′, tetragonal t″, or cubic. Stable monoclinic and rhombohedral phases were not detected for any composition. The discrepancy between our observation and previous results reported by Yashima and co-workers,[1,3] who detected monoclinic and rhombohedral phases for powders with large average sizes, indicates that the phases retained in $ZrO_2-Sc_2O_3$ materials strongly depend on the crystallite size.

For samples calcined at 850 °C, with average crystallite size of $\langle D \rangle = (25 \pm 2)$ nm, our analysis of SXPD data indicated the presence of traces of monoclinic phase for Sc_2O_3 contents of 1 and 2 mol % (not analyzed here by Rietveld refinements), whereas all with higher Sc_2O_3 content were single-phased.

The lattice parameters determined by Rietveld analysis of SXPD data for powders calcined at 650 °C ($\langle D \rangle = 10$ nm) and 850 °C ($\langle D \rangle = 25$ nm) are reported in Figure 1 and Tables 1 and 2, respectively. In both cases, a continuous decrease of the *c*/*a* ratio for increasing Sc_2O_3 content is observed. The t′−t″ compositional boundary occurs when *c*/*a* becomes equal to unity ($c/a = 1$), and this happens at (9 ± 1) mol % Sc_2O_3 for both set of samples. A similar t′−t″ compositional boundary has been reported in the literature for other ZrO_2-based systems doped with trivalent cations.[1] In spite of these similarities, it can be observed that both sets of samples exhibit differences in the lattice parameters and the *c*/*a* ratio as functions of Sc_2O_3 content. Particularly, it can be observed that the *c*/*a* ratio is smaller for samples with $\langle D \rangle = 10$ nm. Furthermore, we can notice in Figure 1 that the transition t′−t″ is sharper for samples with $\langle D \rangle = 25$ nm. The t′−t″ boundary for samples with $\langle D \rangle = 10$ nm is less defined and probably occurs at a Sc_2O_3 content slightly lower than in the case of samples with $\langle D \rangle = 25$ nm. These differences observed for samples with different average crystallite size are typical of ZrO_2-based materials. For example, in pure ZrO_2 nanopowders exhibiting the tetragonal phase, it has been found that the *c*/*a* ratio decreases for decreasing $\langle D \rangle$,[8] in qualitative agreement with our results.

The t″−cubic compositional boundary corresponds to the composition for which *z*(O) reaches its value in fluorite-type structures, i.e., $z(O) = 0.25$. The *z*(O) coordinate was determined for all studied compositions by monitoring the *I*(112)/*I*(111) ratio

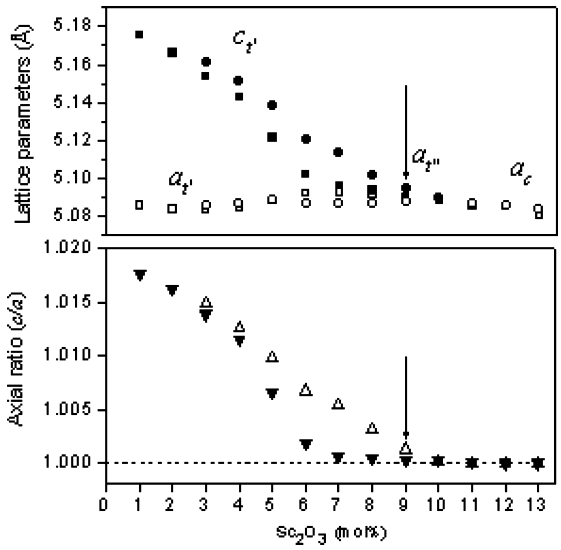

Figure 1. Top: lattice parameters (a and c) as functions of Sc_2O_3 content for powders calcined at 650 and at 850 °C, with $\langle D\rangle = 10$ nm (■, □) and $\langle D\rangle = 25$ nm (●, ○), respectively. The error bars are approximately equal to symbol sizes. Bottom: axial ratio, c/a, as a function of Sc_2O_3 content for both sets of samples (▼calcined at 650 °C, Δ calcined at 850 °C). The t′−t″ compositional boundary is indicated by an arrow.

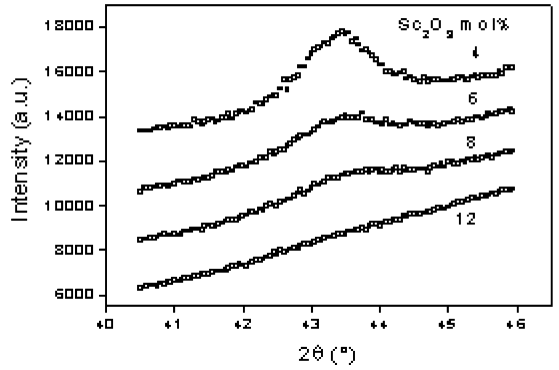

Figure 2. Profiles of the 112 Bragg peak for different $ZrO_2-Sc_2O_3$ compositions calcined at 650 °C ($\langle D\rangle = 10$ nm).

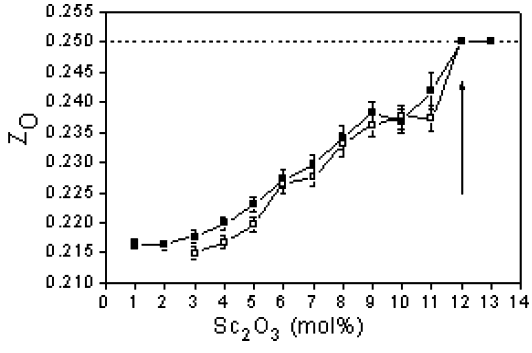

Figure 3. Fractional z-coordinate of the O^{2-} ion in the asymmetric unit of the tetragonal unit cell, z(O), as a function of the Sc_2O_3 content for powders calcined at 650 °C (■, $\langle D\rangle = 10$ nm) and at 850 °C (□, $\langle D\rangle = 25$ nm). The t″−cubic compositional boundary is indicated by an arrow.

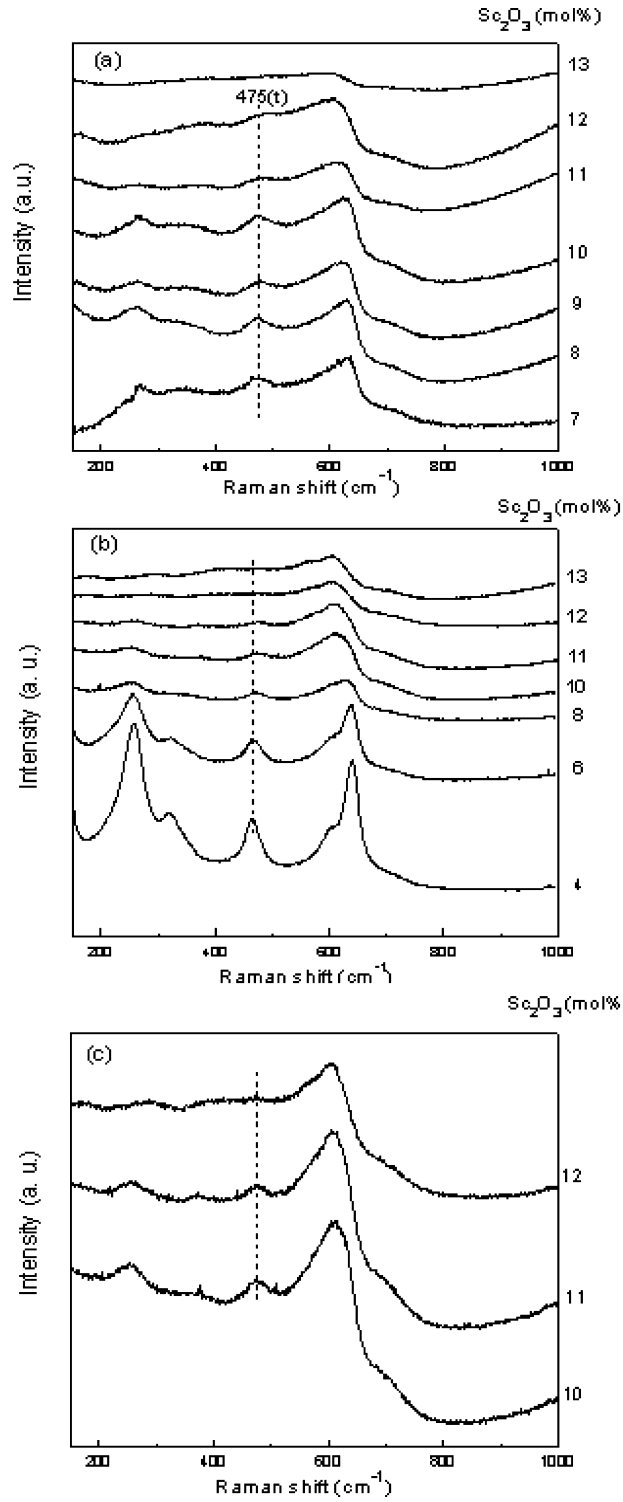

Figure 4. Raman spectra of selected $ZrO_2-Sc_2O_3$ nanopowders calcined at (a) 650 °C ($\langle D\rangle = 10$ nm) and (b) 850 °C ($\langle D\rangle = 25$ nm). (c) Detail for compositions close to the t″−cubic compositional boundary corresponding to samples with average crystallite size $\langle D\rangle = 25$ nm. The dashed vertical lines indicate the position of the band that corresponds to E_g Raman-active mode of the tetragonal phase (475 cm^{-1}).

and applying eq 1. Figure 2 displays typical profiles of the 112 Bragg peak for selected samples calcined at 650 °C ($\langle D\rangle = 10$ nm), showing that the intensity of this peak decreases for increasing Sc_2O_3 content and is negligible for the ZrO_2-12 mol % Sc_2O_3 solid solution. The results plotted in Figure 3 indicate that z(O) progressively increases for increasing Sc_2O_3 content and becomes equal to 0.25 for 12 mol % Sc_2O_3 content, at which I(112) vanishes. The same features were established for samples calcined at 850 °C ($\langle D\rangle = 25$ nm). Again, although small differences in the values of z(O) can be noticed in Tables 1 and

TABLE 1: Structural Parameters and Standard Agreement Factors Obtained from Rietveld Analysis of SXPD Patterns of $ZrO_2-Sc_2O_3$ Nanopowders Calcined at 650 °C ($\langle D \rangle = 10$ nm)[a]

Sc_2O_3 content (mol %)	space group	a (Å)	c (Å)	z(O)	B(Zr, Sc)	B(O)	R_p	R_{wp}	R_{exp}	χ^2
1	$P4_2/nmc$	5.08561(7)	5.17574(8)	0.2164 (8)	0.60(2)	1.29(7)	4.41	6.36	1.73	3.7
2	$P4_2/nmc$	5.08373(6)	5.16606(8)	0.2163 (8)	0.55(2)	1.15(7)	4.25	5.8	1.8	3.2
3	$P4_2/nmc$	5.08315(7)	5.15371(9)	0.218 (1)	0.58(2)	1.32(7)	4.1	5.64	1.81	3.1
4	$P4_2/nmc$	5.08427(7)	5.1424(1)	0.220 (1)	0.62(2)	1.37(7)	4.48	6.05	1.8	3.4
5	$P4_2/nmc$	5.0881(1)	5.1215(2)	0.223 (1)	0.60(3)	1.44(8)	4.43	5.94	1.85	3.2
6	$P4_2/nmc$	5.0923(3)	5.1018(5)	0.227(2)	0.79(3)	1.63(9)	4.72	6.46	1.9	3.4
7	$P4_2/nmc$	5.0927(3)	5.0959(6)	0.230 (2)	0.86(3)	1.76(9)	5.12	7.02	1.88	3.7
8	$P4_2/nmc$	5.0911(4)	5.0935(8)	0.234 (2)	0.90(3)	1.9(1)	5.42	7.33	1.91	3.8
9	$P4_2/nmc$	5.0889(5)	5.09034(9)	0.238 (2)	0.98(3)	2.0(1)	5.73	7.65	2.03	3.8
10	$P4_2/nmc$	5.0879(4)	5.0889(8)	0.237 (2)	0.90(3)	1.6(1)	6.6	8.44	1.98	4.3
11	$P4_2/nmc$	5.0851(4)	5.0857(9)	0.242 (3)	0.97(3)	1.7(1)	6.99	8.92	2.02	4.4
12	$Fm3m$	5.0850(1)			1.22(3)	2.94(8)	6.34	8.54	2.04	4.2
13	$Fm3m$	5.0805(1)			1.32(4)	2.9(1)	7.13	9.24	2.14	4.3

[a] The coordinate z(O) was determined by applying eq 1.

TABLE 2: Structural Parameters and Standard Agreement Factors Obtained from Rietveld Analysis of SXPD Patterns of $ZrO_2-Sc_2O_3$ Nanopowders Calcined at 850 °C ($\langle D \rangle = 25$ nm)[a]

Sc_2O_3 content (mol %)	space group	a (Å)	c (Å)	z(O)	B(Zr, Sc)	B(O)	R_p	R_{wp}	R_{exp}	χ^2
3	$P4_2/nmc$	5.08596(4)	5.16160(4)	0.215 (1)	0.40(2)	1.30(8)	6.3	8.91	1.97	4.5
4	$P4_2/nmc$	5.08654(4)	5.15078(4)	0.217 (1)	0.45(2)	1.43(7)	6.22	7.92	1.94	4.1
5	$P4_2/nmc$	5.08838(4)	5.13810(9)	0.220 (1)	0.26(3)	1.4(1)	7.52	9.56	1.87	5.1
6	$P4_2/nmc$	5.08653(4)	5.12067(5)	0.226 (2)	0.57(2)	1.823(8)	7.44	9.13	2.15	4.2
7	$P4_2/nmc$	5.08647(5)	5.11366(6)	0.228 (2)	0.61(2)	1.7(1)	9.51	11.6	2.07	5.6
8	$P4_2/nmc$	5.08627(4)	5.10183(6)	0.233 (2)	0.84(2)	2.33(8)	7.21	8.61	2.13	4.0
9	$P4_2/nmc$	5.08791(6)	5.0943(1)	0.236 (2)	0.84(2)	2.36(8)	7.03	8.51	2.31	3.7
10	$P4_2/nmc$	5.0894(3)	5.0898(6)	0.238 (2)	0.97(2)	2.62(7)	6.73	8.23	2.25	3.7
11	$P4_2/nmc$	5.08628(3)	5.08628(3)	0.237 (2)	1.12(2)	2.8(4)	8.07	10	2.42	4.1
12	$Fm3m$	5.08583(3)			1.08(2)	2.77(8)	9.41	11	2.34	4.7
13	$Fm3m$	5.08386(4)			1.33(3)	3.22(9)	9.81	11.1	2.42	4.6

[a] The coordinate z(O) was determined by applying eq 1.

2 for samples with $\langle D \rangle = 10$ nm and $\langle D \rangle = 25$ nm, respectively, the same phases were identified for all compositions in both samples.

The phases identified by SXPD were also analyzed by Raman spectroscopy. Figure 4 displays Raman spectra for selected compositions, particularly those close to the tetragonal−cubic boundary (t″−cubic boundary, according to SXPD analysis). No bands of monoclinic or rhombohedral phases were detected. This is an important information because Raman spectroscopy is a very precise technique for detection of traces of these phases.[13,14] By monitoring the band at 475 cm^{-1}, which corresponds to E_g Raman-active mode of the tetragonal phase,[3] we determined the tetragonal−cubic compositional boundary, resulting of (12 ± 1) mol % Sc_2O_3 for both sets of samples (calcined at 650 or 850 °C), in agreement with SXPD results.

Phase Transitions at High Temperature in ZrO_2-10 mol % Sc_2O_3. Phase transitions of ZrO_2-10 mol % Sc_2O_3 powder calcined at 850 °C ($\langle D \rangle = 25$ nm) as a function of temperature were also studied by SXPD. These measurements were performed on cooling from 900 °C. The results displayed in Figure 5 clearly indicate that the integral of the 112 Bragg peak decreases progressively for higher temperature and becomes very weak at 900 °C.

Since in this work we have studied phase transitions maintaining an invariant average crystallite size, the SXPD analysis was not performed for temperatures above 900 °C. At these temperatures, nanocrystal growth and degradation of the compositional homogeneity are expected. Therefore, the temperature of the t″−cubic phase transition was determined by extrapolating to zero the integral of the 112 Bragg peak.

As shown in Figure 6, z(O) increases for increasing temperature, approaching to its value in the cubic phase, z(O) = 0.25.

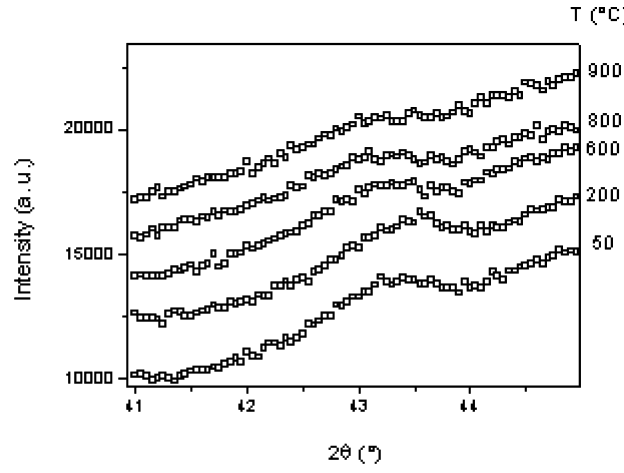

Figure 5. Profile of the 112 Bragg peak as a function of temperature during the cooling cycle from 900 °C, corresponding to the ZrO_2-10 mol % Sc_2O_3 solid solution calcined at 850 °C ($\langle D \rangle = 25$ nm).

The critical temperature of the t″ ↔ cubic transition of the ZrO_2-10 mol % Sc_2O_3 solid solution with $\langle D \rangle = 25$ nm was determined by extrapolating z(O) toward z(O) = 0.25, under the assumption of a simple quadratic temperature dependence. In this way, the t″ ↔ cubic phase transition was determined to be 1340 °C.

Metastable Phase Diagram of Nanocrystalline $ZrO_2-Sc_2O_3$ Solid Solutions. The high-temperature phase transitions of ZrO_2-8 and −11 mol % Sc_2O_3 solid solutions with $\langle D \rangle = 25$ nm were previously investigated by using the procedure explained above.[5] It was established that the ZrO_2-8 mol % Sc_2O_3 solid solution exhibits a t′ ↔ t″ transition at

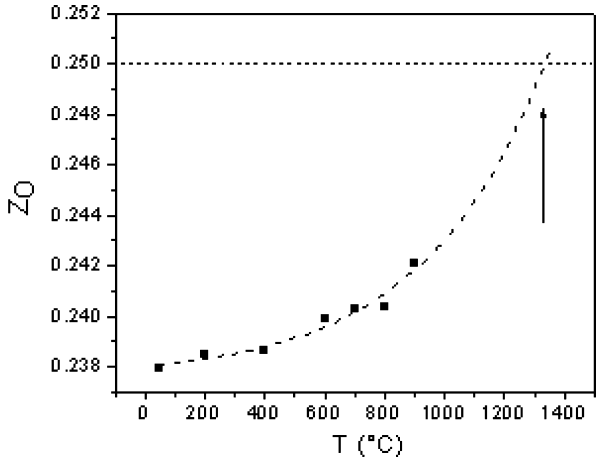

Figure 6. z(O) as a function of temperature for the ZrO_2-10 mol % Sc_2O_3 solid solution calcined at 850 °C ($\langle D\rangle = 25$ nm). The arrow indicates the critical temperature of the t″ ↔ cubic phase transition.

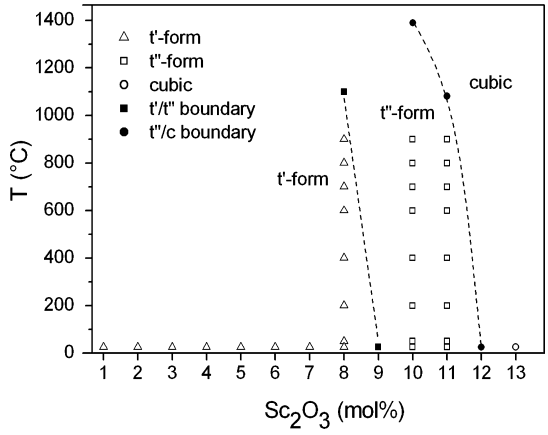

Figure 7. Proposed metastable phase diagram of compositionally homogeneous and nanostructured $ZrO_2-Sc_2O_3$ solid solutions with an average crystallite size $\langle D\rangle = 25$ nm.

1100 °C, whereas the ZrO_2-11 mol % Sc_2O_3 solid solution presents a t″ ↔ cubic transition at 1080 °C. Taking into account these previous results and the new results reported here, corresponding to phases identified at room temperature as a function of Sc_2O_3 content and high-temperature phase transitions of ZrO_2-10 mol % Sc_2O_3 solid solution, we have built up the metastable phase diagram depicted in Figure 7 for nanostructured solid solutions with an average crystallite size of $\langle D\rangle =$ 25 nm.

The metastable phase diagram displayed in Figure 7 for nanocrystalline and compositionally homogeneous $ZrO_2-Sc_2O_3$ solid solutions is very different from the phase diagram proposed by Yashima et al. for materials treated at high temperatures,[1] i.e., with crystallite sizes much larger than the nanopowders studied here. Thus, our results indicate that the retention of metastable phases observed by us is clearly favored in small crystallites, in the nanometric range.

Interestingly, in spite of clear differences reported between the equilibrium phase diagram of the $ZrO_2-Sc_2O_3$ system[2] and those corresponding to other ZrO_2-based materials doped with trivalent cations,[1] the metastable phase diagram reported here for nanocrystalline compositionally homogeneous $ZrO_2-Sc_2O_3$ solid solutions is qualitatively very similar to those corresponding to $ZrO_2-Y_2O_3$ and $ZrO_2-Er_2O_3$ solid solutions with large crystallite sizes.[1] But, differently from these materials, coarse-grained compositionally homogeneous $ZrO_2-Sc_2O_3$ solid solutions exhibit the β rhombohedral phase in the range from 10 to 12 mol % Sc_2O_3, whereas this phase is absent in the nanocrystalline solid solutions studied here.

The suppression of the rhombohedral β phase in favor of the t″-form of the tetragonal phase for small (nanometric) crystallites is not clearly understood yet. In other fine-grained or nanocrystalline systems, different competing theories have been proposed, including lack of nucleation, internal pressure due to particle curvature, surface free energy difference between polymorphs, etc. Particularly, this last mechanism has been proposed by Garvie for the retention of the tetragonal phase in nanocrystalline ZrO_2-based materials.[15,16] In the case of $ZrO_2-Sc_2O_3$ nanopowders studied here, the same mechanism should be considered to explain the retention of the t″-form. In order to quantitatively address this issue, computer calculations of free energies for clusters of both (t″ and β) phases, as functions of crystallite size, are under way.

Conclusions

Single-phased compositionally homogeneous $ZrO_2-Sc_2O_3$ nanopowders, exhibiting metastable forms of the tetragonal phase or the cubic one, were synthesized by a gel−combustion route. The t′−t″ and t″−cubic compositional boundaries at room temperature of nanopowders with average crystallite sizes $\langle D\rangle = 10$ nm and $\langle D\rangle = 25$ nm were determined by SXPD analysis to be at (9 ± 1) and (12 ± 1) mol % Sc_2O_3, respectively.

The high-temperature behavior of the ZrO_2-10 mol % Sc_2O_3 solid solution calcined at 850 °C, with $\langle D\rangle = 25$ nm, was also analyzed by SXPD at varying temperatures. The t″ ↔ cubic transition was established to be at 1340 °C. Taking into account these results and those previously reported for $ZrO_2-Sc_2O_3$ samples with 8 and 11 mol % Sc_2O_3,[5] we have built up the metastable phase diagram of compositionally homogeneous $ZrO_2-Sc_2O_3$ nanopowders with an average crystallite size of $\langle D\rangle = 25$ nm and Sc_2O_3 contents up to 13 mol %.

Interestingly, we have established that the t″-form, with $c/a = 1$, is retained in nanocrystalline $ZrO_2-Sc_2O_3$ solid solutions, whereas this form was not observed in $ZrO_2-Sc_2O_3$ powders with large crystallite size. This tetragonal form has been observed in other ZrO_2-based materials, but this different behavior between nanocrystalline and coarse-grained materials has not been found in other systems. By analyzing a number of $ZrO_2-Sc_2O_3$ samples with progressively increasing average crystallite size, we are now trying to characterize the transition regime from the metastable phase diagram displayed in Figure 7, for nanopowders, toward the phase diagram reported by Yashima et al. for coarse-grained materials.[1] This work is currently in progress.

Acknowledgment. This work was supported by the Brazilian Synchrotron Light Laboratory (LNLS, Brazil, proposals D10B-XPD-5364, 6723, and 7296), scientific collaboration agreements CNPq-CONICET and CAPES-SECyT (Brazil−Argentina), CNPq (Brazil, PROSUL projects nos. 490289/2005-3 and 490580/2008-4), Agencia Nacional de Promoción Científica y Tecnológica (Argentina, PICT 2003 no. 14268, PICT 2005 no. 38309, and PICT 2007 no. 01152), CONICET (Argentina, PIP no. 6559), and Latin-American Centre for Physics (CLAF). Paula M. Abdala thanks CONICET and Fundación YPF for her doctoral fellowship.

Supporting Information Available: SXPD data for ZrO_2-5, −10, and −13 mol % Sc_2O_3 nanopowders calcined at 650 °C. This material is available free of charge via the Internet at http://pubs.acs.org.

References and Notes

(1) Yashima, M.; Kakihana, M.; Yoshimura, M. *Solid State Ionics* **1996**, *86−88*, 1131.

(2) Ruh, R.; Garrett, H. J.; Domagala, R. F.; Patel, V. A. *J. Am. Ceram. Soc.* **1977**, *60*, 399.

(3) Fujimori, H.; Yashima, M.; Kakihana, M. *J. Am. Ceram. Soc.* **1998**, *81*, 2885.

(4) Xu, G.; Zhang, Y. W.; Liao, C. S.; Yan, C. H. *Phys. Chem. Chem. Phys.* **2004**, *6*, 5410.

(5) Abdala, P. M.; Lamas, D. G.; Fernández de Rapp, M. E.; Walsöe de Reca, N. E.; Craievich, A. F.; Fantini, M. C. A. *Powder Diffr.* **2008**, *23*, S87.

(6) Furlan Ferreira, F.; Granado, E.; Carvalho, W., Jr.; Kycia, S.; Bruno, D.; Droppa, R., Jr. *J. Synchrotron Radiat.* **2006**, *13*, 46.

(7) Lamas, D. G.; Fuentes, R. O.; Fábregas, I. O.; Fernández de Rapp, M. E.; Lascalea, G. E.; Casanova, J. R.; Walsöe de Reca, N. E.; Craievich, A. F. *J. Appl. Crystallogr.* **2005**, *38*, 867.

(8) Lamas, D. G.; Rosso, A. M.; Suarez Anzorena, M.; Fernández, A.; Bellino, M. G.; Cabezas, M. D.; Walsöe de Reca, N. E.; Craievich, A. F. *Scr. Mater.* **2006**, *55*, 553.

(9) Fábregas, I. O.; Lamas, D. G.; Walsöe de Reca, N. E.; Fantini, M. C. A.; Craievich, A. F.; Prado, R. J. *J. Appl. Crystallogr.* **2008**, *41*, 680.

(10) Klug, H.; Alexander, L. *X-ray Diffraction Procedures for Polycrystalline and Amorphous Materials*; John Wiley: New York, 1974; p 618.

(11) Rodríguez-Carvajal, J. *FullProf. 98*, version 0.2.; Laboratoire Leon Brillouin (CEA-CNRS): Saclay, France, 1998.

(12) Lee, W. E.; Rainforth, W. M. *Ceramic Microstructures: Property Control by Processing*; Chapman & Hall: London, 1994; p 317.

(13) Djurado, E.; Bouvier, P.; Lucazeau, G. *J. Solid State Chem.* **2000**, *149*, 399.

(14) Fujimori, H.; Yashima, M.; Kakihana, M.; Yoshimura, M. *J. Appl. Phys.* **2002**, *91*, 6493.

(15) Garvie, R. C. *J. Phys. Chem.* **1965**, *69*, 1238.

(16) Garvie, R. C. *J. Phys. Chem.* **1978**, *82*, 218.

JP904584E